

Algorithm-Supervised Millimeter Wave Indoor Localization using Tiny Neural Networks

Anish Shastri, *Graduate Student Member, IEEE*, Steve Blandino, Camillo Gentile, *Member, IEEE*,
Chiehping Lai, *Member, IEEE*, Paolo Casari, *Senior Member, IEEE*

Abstract—The quasi-optical propagation of millimeter-wave (mmWave) signals enables high-accuracy localization algorithms that employ geometric approaches or machine learning models. However, most algorithms require information on the indoor environment, may entail the collection of large training datasets, or bear an infeasible computational burden for commercial off-the-shelf (COTS) devices. In this work, we propose to use tiny neural networks (NNs) to learn the relationship between angle difference-of-arrival (ADoA) measurements and locations of a receiver in an indoor environment. To relieve training data collection efforts, we resort to an algorithm-supervised approach by bootstrapping the training of our neural network through location estimates obtained from a state-of-the-art localization algorithm. We evaluate our scheme via mmWave measurements from indoor 60-GHz double-directional channel sounding. We process the measurements to yield dominant multipath components, use the corresponding angles to compute ADoA values, and finally obtain location fixes. Results show that the tiny NN achieves sub-meter errors in 74% of the cases, thus performing as good as or even better than the state-of-the-art algorithm, with significantly lower computational complexity.

I. INTRODUCTION

Millimeter-wave (mmWave) signals are characterized by wide bandwidth and are transmitted via directional arrays. These characteristics are ideal to provide accurate range and angle information, which are essential for precise localization [1]. In fact, mmWave signals propagate quasi-optically: they reflect off surfaces and obstacles almost specularly, with minimum scattering and diffraction, and are short-ranged due to small antenna aperture and high atmospheric attenuation. The typically sparse channels that result include a dominant line-of-sight (LoS) path and a few non-line-of-sight (NLoS) paths, which can often be mapped to the scatterer that generated them to achieve high-accuracy localization and environment mapping [2].

Manuscript received xxxx xx, xxxx ...

A. Shastri and P. Casari are with DISI, University of Trento, 38123 Povo (TN), Italy (emails: anish.shastri@unitn.it, paolo.casari@unitn.it).

S. Blandino is research associate with the National Institute of Standards and Technology (NIST), Gaithersburg, MD 20899 USA, and contractor with Prometheus Computing LLC, Bethesda, MD 20814 USA (email: steve.blandino@nist.gov).

C. Gentile (email: camillo.gentile@nist.gov) and C. Lai (e-mail: chiehping.lai@nist.gov) are with the Radio Access and Propagation Metrology Group, National Institute of Standards and Technology, Gaithersburg, MD 20899 USA.

This work received support from the European Commission's Horizon 2020 Framework Programme under the Marie Skłodowska-Curie Action MINTS (GA no. 861222), and was partially supported by the European Union under the Italian National Recovery and Resilience Plan (NRRP) of NextGenerationEU, partnership on "Telecommunications of the Future" (PE00000001 - program "RESTART").

U.S. Government work, not subject to U.S. Copyright.

mmWave signals attenuate over short distances and humans are their most significant blockers indoors [3]. Hence, dense access point (AP) deployments will be inevitable to provide uniform coverage and support next-generation applications requiring multi-Gbit/s data rates such as virtual reality (VR), 4K video streaming, and indoor robot navigation [4], [5]. In this scenario, accurate localization helps optimize the performance of mmWave networks by designing optimized beam training protocols [6], or prevent blockage events by triggering timely handovers [7]. Moreover, device-centric algorithms lead to better scalability in dense mmWave networks and help reduce the network maintenance overhead, increase spatial reuse, and enable load balancing and medium access control (MAC)-level communication scheduling [8].

Localization schemes should cater for the computational constraints of commercial off-the-shelf (COTS) devices and work with existing mmWave communication equipment, with no need for extra sensors [9], [10]. Yet, current approaches tend to cluster into one of the following categories: either *i*) they employ large neural network (NN) models to process mmWave radio features and output a location estimate, or *ii*) solve complex geometric and optimization problems. In case *i*), the resulting algorithms may fit COTS devices, but require an often burdensome training data collection phase. In case *ii*), the algorithms may make strong assumptions related to environment knowledge (e.g., they may assume to know the absolute orientation of the devices), or their complexity may grow super-linearly with the number of measurements collected. In both cases, the algorithm may become impractical in realistic scenarios.

In this work, we propose to bridge the above gap by means of an algorithm-supervised indoor localization approach. To keep complexity minimal, we resort to a tiny NN model that exploits angle difference-of-arrival (ADoA) information as input features. Such NN models have much fewer weights compared to other architectures in the literature, thus being compatible with resource-constrained COTS hardware. To relieve the effort of collecting training data for the NN, we initially resort to a bootstrapping localization algorithm based on the same ADoA data we feed to the NN. While such algorithm will inevitably make errors when computing location estimates, it will still yield approximate location labels for ADoA readings, which can work as training data for the tiny NN. In any event, the advantage of not having to explicitly collect training data largely offsets the disadvantage of imperfect location labels in any practical scenario. As each mmWave device localizes itself, our scheme is *device-centric*, hence more scalable than AP-centric approaches [5].

We choose JADE as the bootstrapping¹ algorithm. JADE is a state-of-the-art geometric approach from the literature [11] that uses ADoA information to solve a grid search optimization and two iterative minimum mean-square error (MMSE) problems. It jointly localizes a mmWave device and all surrounding physical and virtual APs,² without any prior information about the environment (number of APs, room boundaries, etc).

We evaluate the performance of our approach using channel measurements, recorded with a high-precision 3D double-directional 60-GHz channel sounder throughout four different transmitter locations and one mobile receiver, totaling >10 000 measurements in a fully furnished work environment. The rich output of the sounding process includes numerous multipath components (MPCs), which cannot be directly used for localization purposes. Different from previous approaches [12], [13], we pre-process and filter such output. There are two reasons why this is necessary. First, the wealth of sensed MPCs makes it challenging to associate them to ambient scatterers. This is critical, as wrong associations may jeopardize the localization process. Second, while the LoS path and first-order reflections yield the majority of the received energy, diffuse paths scattered from rough surfaces may also bear non-negligible energy. Therefore, we need to identify them out of the remaining MPCs.

This paper substantially extends our previous work [13], which proposed shallow NN models working in simple, simulated indoor environments. In this paper, we employ NNs that apply to more realistic scenarios, and validate their performance using real channel measurements. Moreover, we provide additional simulation results that show how location errors distribute across an indoor space in different conditions.

The specific contributions of our work are:

a) We propose a tiny, computationally-lightweight NN model that estimates the location of a mmWave device by leveraging ADoA measurements obtained from estimated multipath components at the receiver.

b) We reduce the training dataset collection overhead via an algorithm-supervised approach: we train the NN model using error-prone location estimates from a bootstrapping geometric scheme that also exploits ADoAs; once trained, we only use the NN for localization.

c) We evaluate our approach using a rich mmWave channel sounding dataset collected at NIST Boulder’s campus [14], which we extensively process. In particular, we propose a recursive clustering algorithm based on density-based spatial clustering of applications with noise (DBSCAN) to distinguish the dominant LoS MPC from first-order-reflected MPCs and the diffused MPCs.

d) We complement our evaluation with additional simulation results from a complex-shaped room environment.

The remainder of this paper reviews indoor mmWave localization techniques (§II); describes our proposed algorithm (§III) and the experimental data used to validate it (§IV); and

discusses experimental and simulation results (§V). Finally, §VI concludes the paper.

II. RELATED WORK

A. Conventional localization and mapping algorithms

Location systems based on mmWave technology employ one or more signal parameters to estimate the location of a device [5], [15]. Schemes relying on received signal strength indicator (RSSI) and/or signal-to-noise ratio (SNR) information typically infer the distance between the device and the known anchors by inverting indoor path loss models. For instance, in [16] the authors propose trilateration-based localization using RSSI measurements for a 60 GHz IEEE 802.11ad network.

Most of the algorithms based on angle information employ geometric techniques [5]. The simplest schemes triangulate the receiver using angle of arrivals (AoAs) from multiple transmitters, or compute ADoAs across different MPC pairs to localize a device [17], [18]. In [11], the authors propose JADE, a scheme that jointly localizes both the devices and the APs, and then reconstructs the likely location of reflective surfaces in the environment. The scheme requires multiple iterations before location estimates converge, and needs ADoA measurements from different locations before to be accurate. New ADoA measurements help refine previous location estimates. However, the complexity of JADE increases quadratically with the number of measurements, making it too complex to be implemented on resource-constrained COTS devices. Blanco *et al.* exploit AoA and time of flight (ToF) measurements from 60-GHz 802.11ad-based routers as well as sub-6 GHz equipment to trilaterate the location of a client [19].

The AP-centric localization algorithm in [7] exploits channel state information (CSI) measurements from a client to infer angle information, and thus the client’s location. Location estimates were then employed to enhance handover decisions and beam pattern selection. A map-assisted positioning technique to localize a device was proposed in [20] and evaluated using a 3D ray tracer at 28 GHz and 73 GHz. Yassin *et al.* worked on localization and mapping schemes based on context inference, obstacle detection and classification using geometric techniques [21]–[23]. The scheme in [24] uses the beam training procedure to acquire AoAs, employs ADoAs to localize the mmWave device and all the anchors to simultaneously map the environment. The scheme is experimentally evaluated on 60 GHz mmWave hardware. In [25], the authors leverage coarse-grained per-beampattern SNR measurements provided by a modified firmware flashed on multiple 802.11ad-compliant routers. Angle of departure (AoD) and SNR were used in [26] to design beam-based midline intersection and beam scaling-based positioning algorithms. These were evaluated using both ray-tracing and WiGig system-on-chip (SoC) transceivers.

B. Machine learning-based algorithms

Several works employed deep learning to localize mmWave devices indoors. For example, a multi-layer perceptron regression model maps the SNR fingerprints to the coordinates of

¹In this work, we refer to bootstrapping as the data annotation technique that automatically obtains labels for the training data.

²Virtual APs appear as the source of NLoS paths originating from a physical AP and reflecting off an obstacle.

a device in one dimension in [27]. Pajovic *et al.* used RSSI and beam index fingerprints to design probabilistic localization models [28] and used spatial beam SNRs in [29] to learn a multi-task model for position and orientation classification. The authors in [30] and [31] proposed ResNet-inspired models for LoS and NLoS scenarios. To tackle NLoS propagation, spatial beam SNR values were used in [30], and multi-channel beam covariance matrix images in [31]. In [32], the authors used the K-nearest neighbours (K-NN) algorithm to localize unmanned aerial vehicles (UAVs) via indoor RSSI-based fingerprinting, whereas AoAs fingerprints together with RSSI measurements at reference locations were used in [33].

Although deep learning schemes yield accurate location estimates, they (a) are not easily scalable, as radio fingerprints change with the number of APs as well as the setup of the indoor environment (furniture, presence of people, etc.); (b) require knowledge of the indoor environment; (c) require large training datasets; (d) require fusing multiple mmWave signal parameters to form rich input feature vectors for the models; (e) rely on models with hundreds of thousands of parameters, which may be infeasible for resource-constrained devices.

C. Summary

The above survey suggests that experimentally evaluated mmWave localization schemes tend to exhibit one of the following limitations: (a) Low-complexity geometric techniques such as in [18] necessitate knowledge of a device’s orientation and environment map. Furthermore, they are vulnerable to imprecise AoA estimates. (b) Geometric schemes that gradually refine location estimates from multiple AoA measurements experience super-linearly high computational complexity as the number of collected measurements increases. (c) Deep learning-based techniques rely on fingerprint datasets, which require a significant training data collection burden (particularly in large and challenging environments); moreover, they may necessitate excessive computational resources. (d) Implementing and deploying these algorithms on resource-constrained COTS devices is challenging.

By way of contrast, our tiny NNs have much fewer parameters to learn, thus have lower computational complexity and can train faster. We avoid collecting ground truth data for our model by bootstrapping the training process via location estimates from a geometric localization algorithm. After training, we switch to the NN model, and do not need the bootstrapping algorithm any longer for the same environment. Our models achieve a good accuracy with real 60 GHz channel measurements, despite training with inherently error-prone labels.

III. PROPOSED LOCALIZATION SCHEME

A. Key idea: algorithm-supervised tiny neural networks

Our key proposition is to localize mmWave devices via a tiny NN, trained to reproduce the behavior of an otherwise complex localization algorithm. Besides the lower computational burden that results, using a bootstrapping algorithm allows us to train the NN in a fully algorithm-supervised

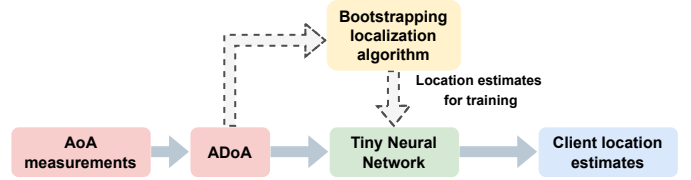


Fig. 1. Workflow of our proposed localization scheme.

fashion, with no need for the typically heavy process of collecting training data.

Fig. 1 shows the workflow of our proposed localization scheme. We assume that the SNR between the transmitter and receiver is sufficient to achieve over-the-air synchronization. We start by computing ADoAs from the set of MPCs of the mmWave channel at a given location, by taking the AoA of one MPC as a reference. A tiny NN model then learns a non-linear regression function, mapping the input ADoA values to the 2D coordinates of the receiver. As training is algorithm-supervised via a bootstrapping localization algorithm, the association between ADoA and the location where these ADoAs are observed will be inherently error-prone. Note that classification models, which would return the best-matching location from a training database for each set of measured ADoAs, would be inherently less robust to error-prone training data than regression NN models [13], besides requiring a much larger NN output stage with inherently coarse location resolution. In fact, algorithm-supervised training with error-prone location labels is advantageous in our case, both from a practical standpoint (because it removes the need for training data collection) and from an accuracy standpoint.

B. Input features of the NN

We employ ADoA values computed from the AoAs of the MPCs of the channel extracted by the receiver, to localize mmWave devices.³ This removes the compass bias at the receiver, thus making localization problem invariant to RX orientation [17]. Note that this procedure is amenable both to lab-grade devices [12], [24] and COTS devices [7], [25].

The set of MPCs that reach the receiver typically includes one LoS path and multiple NLoS paths. NLoS paths can be modeled as emanating from a (virtual) source that corresponds to the mirror image of the physical TX with respect to a reflective surface. We refer to these sources as virtual TXs, and collectively call physical and virtual TXs *anchors*. Fig. 2 illustrates one virtual anchor (VA) for the TX, representing the source of the NLoS path.

After extracting the MPCs from each available TX, we elect one reference MPC and compute ADoAs with respect to the AoA of that MPC. The reference MPC can be the LoS path or a NLoS path from any transmitter. Once we collect AoA

³We neglect the MPC delay as the input to both the schemes, as most commercially deployed indoor mmWave systems such as IEEE 802.11ad/ay wireless LAN (WLAN) systems require additional CSI pre-processing steps in order to retrieve the MPC delays, unlike the AoAs. While there exist standards for estimating the time of flight, e.g., via the fine time measurement (FTM) protocol (IEEE 802.11-REVmc), these methods generally estimate the delay corresponding to the strongest path between the transmitter (TX) and the receiver (RX), which can be either a LoS or NLoS path.

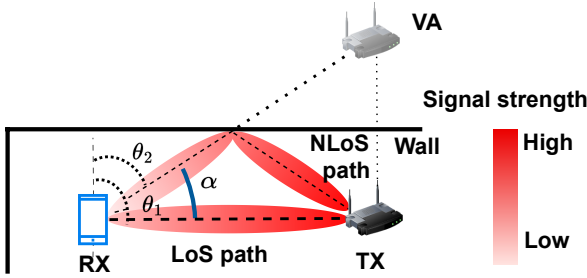


Fig. 2. Illustration of virtual anchor and first-order reflections. Here, θ_1 and θ_2 represent the AoAs of the LoS and the NLoS paths, and $\alpha = \theta_1 - \theta_2$ represents the ADoA with respect to the LoS path. Note that first-order reflections have the same geometrical properties (delay and AoA) of direct rays generated from virtual anchors.

measurements from all N_a anchors, we obtain $N_a - 1$ ADoA values, which are employed as the input features to our NN.

Although the LoS and specular MPCs account for most of the channel energy, diffuse MPCs arising from rough surface scattering may appear, especially at mmWaves frequencies. The number of MPCs that reach the RX is thus typically larger than the total number of anchors. Hence, mmWave propagation in indoor environments is often modelled through clusters of rays [4], [5], [34]. Similarly, we propose to cluster the MPCs to determine the dominating MPCs reflecting off ambient scatterers (e.g., walls, doors, and the ceiling) and their corresponding AoA. The next subsection presents our approach.

C. Clustering of the multi-path components

Although mmWave signals propagate quasi-optically, diffuse paths can account for up to 40% of the channel energy [14], [34]. Diffuse paths tend to aggregate, forming dense clusters in both the angle and delay domains. Hence, mmWave channel models cluster the MPCs over both domains [35], [36].

We employ clustering to group closely-packed MPCs that reach the receiver. We achieve this through DBSCAN, a density-based algorithm that determines clusters by finding data points lying within a user-defined radius and sharing a given number of neighbors [37]. A data point includes the time delay, azimuthal AoA, and elevation AoA features of the MPCs [38]. Unlike other conventional clustering approaches such as K-means and K-NN, DBSCAN does not require prior information on the number of clusters. It can identify clusters of different shape and size, and can separate dense MPC clusters from sparsely spread-out MPCs. Each cluster formed is likely reflected off different ambient scatterers. As a result, the number of clusters is also an estimate of the number of reflecting surfaces. To manage the few cases where DBSCAN clusters multiple MPCs together upon a single pass, we use DBSCAN recursively. Namely, for each cluster, we re-run the algorithm with a progressively smaller cluster radius, and allowing a smaller number of neighbors in the cluster.

We summarize the clustering procedure in Algorithm 1. Consider data from one TX for now. Call $\mathbf{X}_t = [\boldsymbol{\tau}, \boldsymbol{\theta}, \boldsymbol{\psi}]$ the matrix containing the features of all L_t MPCs that the

RX observes at the t -th location, where the $L_t \times 1$ vectors $\boldsymbol{\tau}, \boldsymbol{\theta}, \boldsymbol{\psi}$ represent the delay (in ns), azimuth, and elevation AoAs (in degrees wrapped in the interval $[0^\circ, 360^\circ)$) of the MPCs, respectively. This yields a similar scale for all values, and does not require additional feature rescaling.

We initially cluster \mathbf{X}_t with DBSCAN, resulting in a set of clusters \mathcal{X}_t (line 2). We compute the centroids using the core points of each cluster in \mathcal{X}_t (i.e., those cluster points that share at least γ neighbors) and store them in set \mathcal{C} (line 3). Then, for each cluster and its centroid, we compute a cost defined as the average Euclidean distance between the centroid and each of cluster's points. If this cost is greater than the cluster radius ϵ (line 4), we remove the centroid of the cluster from set \mathcal{C} (line 7), and re-cluster the points through DBSCAN (line 8), with a radius and number of neighbors scaled down by η (line 5). We then add the centroids of the newly determined clusters back to set \mathcal{C} (lines 10-11).

We repeat the above process until all clusters are composed of points located no farther from the centroid than the cluster radius parameter in the delay-AoA domain. The resulting set of centroids \mathcal{C} corresponds to the dominant MPCs (both LoS, if available, and NLoS) reflected off surfaces or obstacles and observed at the RX location. The presence of multiple points in each cluster represents dispersed/scattered components related to the same MPC [39]. After clustering MPCs from all transmitters t , we group the resulting cluster sets \mathcal{X}_t . The centroids are finally characterized by their mean MPC delay and mean azimuth and elevation AoAs.

We remark that the average complexity of a regular DBSCAN procedure is $\mathcal{O}(N \log N)$, where N is the total number of MPCs obtained from each TX (in the order of few hundreds). On the contrary, the complexity of recursive DBSCAN procedure is $\mathcal{O}(N \log N + K \cdot m \log m)$, where K is the upper-bound average number of clusters to be re-clustered and m is the average number of MPCs in such cluster. As our proposed procedure only breaks down those clusters that have a total associated cost exceeding ϵ , K and m are significantly less than N . Thus, the increase in the average complexity remains relatively insignificant.

Dynamic changes in the environment can affect small-scale fading parameters such as phase and MPC delay [40]. However, recursively clustering these MPCs and subsequently computing the centroids helps average-out these fading effects. As these centroids eventually correspond to the AoAs (and thus, the ADoAs) of the dominant MPCs, our localization schemes can thus be resilient to dynamic environments.

To compute ADoAs, we first choose the reference MPC \bar{c}_{k^*} as the one with the least delay, where $k^* = \arg \min_k \tau_k$ for $k = 1, 2, \dots, |\mathcal{C}|$. We then remove \bar{c}_{k^*} from \mathcal{C} and sort the AoAs of the remaining centroids in increasing order. In practice, this corresponds to sweeping the entire azimuthal angle domain in increasing order of the AoAs (as seen from the global reference frame). We then subtract θ_{k^*} from the sorted AoAs. We finally form the input feature vector for the NN, by expressing all ADoAs in radians wrapped in $[-\pi, \pi)$.

Algorithm 1: Recursive DBSCAN

```

1 Function REC_DBSCAN( $\mathbf{X}$ ,  $\epsilon$ ,  $\gamma$ ,  $\eta$ ):
2    $\mathcal{X} \leftarrow$  DBSCAN( $\mathbf{X}$ ,  $\epsilon$ ,  $\gamma$ )
3    $\mathcal{C} \leftarrow$  CENTROID( $\mathcal{X}$ )
4   while  $\exists \mathbf{X}_c \in \mathcal{X}$  of centroid  $\mathbf{c}$  s.t.
     COST( $\mathbf{X}_c$ ,  $\mathbf{c}$ )  $>$   $\epsilon$  do
5      $\epsilon' \leftarrow \eta\epsilon$ ,  $\gamma' \leftarrow \eta\gamma$ 
6     foreach  $\mathbf{X}_c \in \mathcal{X}$  of centroid  $\mathbf{c}$  s.t.
       COST( $\mathbf{X}_c$ ,  $\mathbf{c}$ )  $>$   $\epsilon'$  do
7        $\mathcal{C} \leftarrow \mathcal{C} \setminus \{\mathbf{c}\}$ 
8        $\mathcal{X}_n \leftarrow$  DBSCAN( $\mathbf{X}_c$ ,  $\epsilon'$ ,  $\gamma'$ )
9       foreach  $\mathbf{X}_n \in \mathcal{X}_n$  do
10         $\mathbf{c}_n \leftarrow$  CENTROID( $\mathbf{X}_n$ )
11         $\mathcal{C} \leftarrow$  Append( $\mathbf{c}_n$ )
12      $\epsilon \leftarrow \epsilon'$ ,  $\gamma \leftarrow \gamma'$ 
13 return  $\mathcal{C}$ 

```

TABLE I
SUMMARY OF THE NUMBER OF NEURONS IN EACH LAYER

| Layer | Number of neurons |
|------------------------------|----------------------------|
| Input layer (N_i) | $N_a - 1$ |
| Hidden layer 1 (N_{h_1}) | $\lceil \kappa N_i \rceil$ |
| Hidden layer 2 (N_{h_2}) | N_{h_1} |
| Hidden layer 3 (N_{h_3}) | $\lceil N_{h_2}/2 \rceil$ |
| Output layer (N_o) | 2 |

D. Architecture of the NN

We propose tiny NNs with four layers. The number of neurons of the first layer matches the maximum number of AoAs we expect, i.e., $N_i = N_a - 1$. The first hidden layer contains $N_{h_1} = \kappa N_i$ neurons. For the second hidden layer, $N_{h_2} = N_{h_1}$, whereas for the third hidden layer we set $N_{h_3} = N_{h_2}/2$. Finally, the output layer consists of two neurons, conveying the regression estimate of the 2D coordinates of the RX. Table I summarizes the number of neurons in each layer, where $\lceil \cdot \rceil$ represents the ceiling function.

We train our NN to learn a non-linear function that maps the input ADoAs to the output RX coordinates. Call \mathbf{x} , the RX location coordinates, $\Theta_{\mathbf{x}}$ the input ADoA vector at location \mathbf{x} , and $\mathbf{W}_i = [\mathbf{w}_1 \cdots \mathbf{w}_{n_i}]$ the weight matrix of layer i , where n_i represents the number of neurons in layer i , and each $n_{i-1} \times 1$ vector \mathbf{w}_j contains the weights of the edges that connect the n_{i-1} neurons in layer $i-1$ to the j th neuron in layer i . Furthermore, let $\mathbf{b}_i = [b_1 \cdots b_{n_i}]^T$ be the vector containing the bias values for each neuron in layer i , and call $\mathcal{A}(\cdot)$ the activation function for each neuron. Then, the output values of layer i can be expressed recursively as

$$\mathbf{y}_i = \mathcal{A}(\mathbf{W}_i^T \mathbf{y}_{i-1} + \mathbf{b}_i), \quad (1)$$

where applying $\mathcal{A}(\cdot)$ to a vector denotes computing the activation function $\mathcal{A}(\cdot)$ for each entry of the vector, and yields the vector of the corresponding results. Note that $\mathbf{y}_0 = \Theta_{\mathbf{x}}$ represents the input to the NN. As our NNs models have $n = 4$

TABLE II
SUMMARY OF THE HYPERPARAMETERS

| Hyperparameter | Range |
|--------------------------|-------------------------|
| Node factor (κ) | {0.6, 0.7, 0.8, 0.9, 1} |
| Dropout rate (p) | {0%, 10%, 15%, 20%} |
| Learning rate (r) | [0.0001, ..., 0.01] |
| Batch size (b) | {50%, 75%} |

layers, the estimated location of the receiver is given by

$$\hat{\mathbf{x}} = [\hat{x}_1, \hat{x}_2]^T = \mathbf{y}_4 = \mathcal{F}(\Theta_{\mathbf{x}}), \quad (2)$$

where

$$\mathcal{F}(\Theta_{\mathbf{x}}) = \mathcal{A}(\mathbf{W}_4^T \mathcal{A}(\mathbf{W}_3^T \mathcal{A}(\mathbf{W}_2^T \mathcal{A}(\mathbf{W}_1^T \Theta_{\mathbf{x}} + \mathbf{b}_1) + \mathbf{b}_2) + \mathbf{b}_3) + \mathbf{b}_4) \quad (3)$$

is the non-linear regression function the NN applies to the ADoAs. As the number of neurons in our NNs is small, computing $\mathcal{F}(\cdot)$ only requires a limited number of small-size matrix multiplications and vector summations. Such operations are feasible even for computationally-constrained devices. We choose the rectified linear unit activation function (ReLU) for $\mathcal{A}(\cdot)$, and train the network using the Adam optimizer. We frame the regression as a mean-square error (MSE) minimization problem, and utilize the MSE loss function

$$\mathcal{L}(\mathbf{x}, \hat{\mathbf{x}}) = |x_1 - \hat{x}_1|^2 + |x_2 - \hat{x}_2|^2, \quad (4)$$

where (x_1, x_2) are the algorithm-supervised location labels for ADoA features from the bootstrapping algorithm, and (\hat{x}_1, \hat{x}_2) are the location estimates yielded by the NN.

E. Hyperparameter tuning

In order to optimize the NN to minimize the loss function, we automatically tune the following hyperparameters of the model: i) the node factor κ , which defines the number of neurons in the hidden layers; ii) the dropout rate p , which helps prevent overfitting by ignoring $p\%$ of the NN links during the training phase; iii) the learning rate r ; and iv) the training data batch size b . Table II summarizes the hyperparameter search ranges. The learning rate values range from 10^{-4} to 10^{-2} in a logarithmic progression, with ten values per decade. The optimal hyperparameters for the NN model are chosen from given set after an exhaustive grid search technique.

F. Choice of the bootstrapping localization algorithm

In our algorithm-supervised approach, the bootstrapping algorithm has two objectives: (i) to localize a device while the NN is not yet trained; (ii) to provide location labels that we can associate to ADoA measurements in order to train the NN. Ideally, the algorithm should work with the same input data as the NN, so that the devices does not need to measure/process additional metrics.

In this work, we choose JADE [11]. Besides employing ADoAs as input, JADE does not require knowledge of the surrounding environment or the location of the TXs, and is designed to jointly estimate both the location of the RX

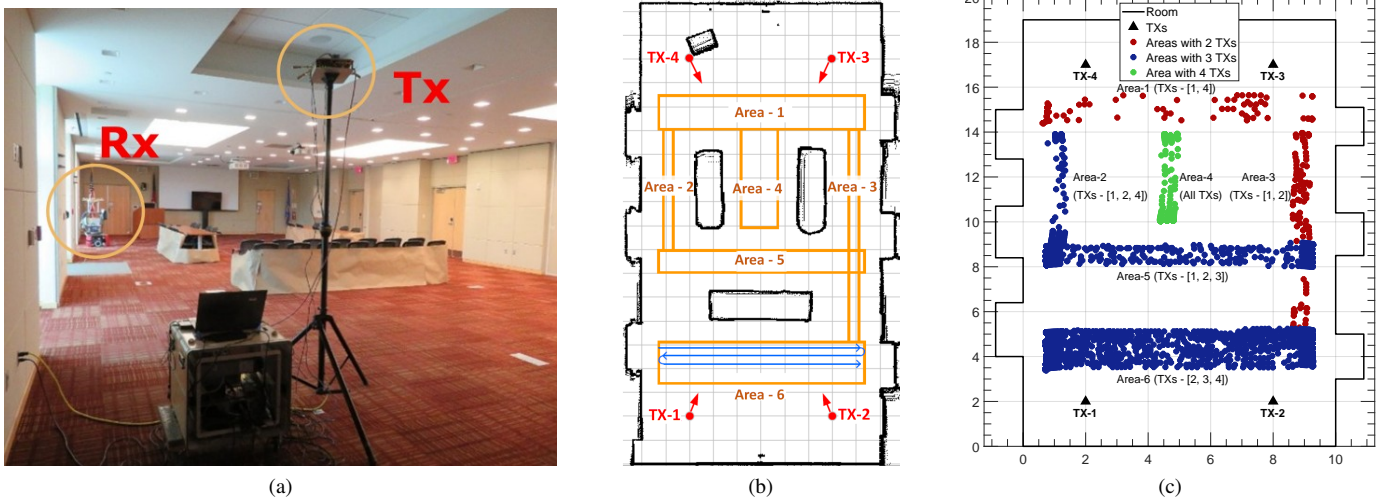


Fig. 3. (a) Measurement setup and (b) floor plan of the room for the 3D double directional 60 GHz channel sounder experiment conducted at NIST to collect indoor mmWave channel responses. (c) Dataset resulting from processing the channel estimation data. The areas are divided and annotated based on the number of TXs from which the RX captures the signal. Axis unit: [m]. Note the different axis scale.

and the location of all physical and virtual TXs. As the RX moves, JADE progressively cumulates additional ADoA measurements, and becomes more accurate at estimating current and the past RX locations, as well as anchor locations. The latter is also the main downside of JADE, as refining past estimates implies a quadratic increase in the complexity of the algorithm with the number of measurements. However, JADE still fits our case perfectly, since its location estimates enable us to train the NN and switch to it well before JADE’s complexity starts escalating [13].

IV. MMWAVE CHANNEL MEASUREMENTS FROM A 60 GHz SOUNDER

To validate our localization scheme in a real indoor environment, we employ an experimental dataset collected at the NIST premises in Boulder, CO, USA. In this section, we describe the dataset collection procedures and the pre-processing steps required to extract ADoAs.

Firstly, we outline the mmWave channel sounder used to capture the channel measurements. We then describe the measurement campaign and the MPC extraction technique. Finally, we discuss the pre-processing steps that yield the ADoAs of the MPCs.

A. Channel sounder

Fig. 3a displays the TX and the RX of the NIST 60 GHz 3D double-directional switched-array channel sounder. The RX embeds a circular array of 16 horn antennas having a 3D Gaussian radiation pattern with 22.5° beamwidth and 18.1 dBi gain. To avoid “blind spots”, the angular spacing between adjacent horns along the array’s azimuthal plane is matched to the beamwidth, i.e., subsequent horns are oriented 22.5° away from each other. Moreover every second horn in the circular array is oriented towards an elevation angle of 22.5° . The resulting synthesized azimuth field-of-view of the array is 360° , whereas the elevation field-of-view (FoV) is 45° .

The TX is almost identical, except that it embeds a semi-circular array with 8 horns, limiting the azimuthal FoV to 180° while maintaining the same 45° -elevation FoV. We synchronously trigger the TX and the RX via rubidium clocks at each end, which are also used to discipline the local oscillators. For further system details, we refer the interested readers to [14], [41].

B. Measurement campaign and MPC extraction

The measurements took place in a $19.3\text{ m} \times 10\text{ m}$ lecture room (Fig. 3b). The TX was installed on a tripod at a height of 2.5 m, whereas the RX was mounted on a mobile robot at a height of 1.6 m. An onboard computer on the robot makes it possible autonomously record channel acquisitions, and a laser-guided navigation system reports the robot’s ground-truth location and heading. The top half of the room in Fig. 3a included two tables with surrounding chairs, while the bottom half included two rows of chairs facing the top wall.

During the measurements, the TX was iteratively placed at the four corners of the room, marked TX-1 to TX-4, and oriented towards the center of the room (indicated by the arrows) in order to optimize the spatial coverage of the mmWave signal. For each TX location, the RX moved along a lawnmower trajectory in each of the measurement areas labeled 1 to 6 at a maximum speed of 2 m/s. The average distance between consecutive recordings was $\sim 9\text{ cm}$, which emulates measurements taken during RX motion. The channel was void of any motion, e.g., humans in the room, except for that of the RX. We recorded 10 895 channels in total.

Each acquisition sequentially measures the channel impulse response (CIR) between each of the 8 TX and each of the 16 RX antennas, resulting in 128 CIRs per acquisition. The 128 CIRs are then coherently combined through the space-alternating generalized expectation maximization (SAGE) super-resolution algorithm [42] to extract MPCs channel paths and their geometric properties. While the SAGE

algorithm de-embedded the directional beam patterns of the antennas, we removed the effects of the TX and RX's front ends via pre-distortion filters [14], [38].

C. Dataset preprocessing

We pre-process the collected dataset to compute ADoAs that can input into our localization scheme. The rationale behind this step is that, ideally, a RX should be able to measure MPCs from all TXs at the same location. Instead, the measurements the RX takes from different TXs are slightly displaced. This is because the robot that moves the receiver needs to be restored to its starting location and start its path anew every time the TX is relocated. To overcome this shortcoming, we seek closest locations where the RX obtained measurements from different transmitters, and coalesce them into a single set of MPCs measured at roughly the same location. For this, we use the range searching technique as follows.

Let $\mathcal{M}_{n,t}^i$ be the set of all locations in area n where the RX takes channel measurements from TX $i \in \mathcal{T}_n$, where \mathcal{T}_n is the set of transmitters available in area n . These locations are indexed by time step $t = 1, 2, \dots, N_n^i$, where N_n^i is the total number of measurement locations for transmitter i in area n . Every location $\mathbf{m}_{n,t}^i \in \mathcal{M}_{n,t}^i$ is a 3D coordinate vector associated with a measurement matrix $\mathbf{\Gamma}_{n,t}^i = [\boldsymbol{\alpha}, \boldsymbol{\tau}, \boldsymbol{\theta}, \boldsymbol{\psi}, \boldsymbol{\phi}, \boldsymbol{\beta}]$ of size $C_{n,t}^i \times 6$, where $C_{n,t}^i$ is the number of MPCs returned by the channel estimation algorithm. In $\mathbf{\Gamma}_{n,t}^i$, $\boldsymbol{\alpha}$ contains the path loss of each MPC (in dB), $\boldsymbol{\tau}$ represents the propagation delay (in ns), $\boldsymbol{\theta}$ and $\boldsymbol{\psi}$ are the azimuth and elevation AoAs at the RX (in degrees), whereas $\boldsymbol{\phi}$ and $\boldsymbol{\beta}$ are the azimuth and elevation AoDs at the TX (in degrees).

To carry out the range search, we first elect a reference TX, e.g., the one with the lowest ID number. Call this TX i^* . Then we start from $t = 1$ and find the closest measurement locations for all remaining available transmitters. Namely, $\forall i \in \mathcal{T}_n \setminus \{i^*\}$, we find

$$u_i^* = \arg \min_{u_i} \|\mathbf{m}_{n,u_i}^i - \mathbf{m}_{n,t}^{i^*}\|. \quad (5)$$

We then cluster the measurement locations as set

$$\mathcal{C}_{n,t} = \{\mathbf{m}_{n,t}^{i^*}\} \cup \left\{ \mathbf{m}_{n,u_i^*}^i, i \in \mathcal{T}_n \setminus \{i^*\} \right\}. \quad (6)$$

Finally, we remove the locations in $\mathcal{C}_{n,t}$ to avoid that they become also part of other sets formed later on, i.e.,

$$\mathcal{M}_{n,t+1}^i = \mathcal{M}_{n,t}^i \setminus \{\mathbf{m}_{n,u_i^*}^i\}. \quad (7)$$

We repeat the above operations for all t , and finally take the centroid of each cluster $\mathbf{c}_{n,t}$ as the closest approximation of a measurement location having data from all TXs in area n , and merge all MPCs from all corresponding measurements in matrix $\mathbf{\Gamma}_{n,t} = [\mathbf{\Gamma}_{n,t}^{i^*} \mathbf{\Gamma}_{n,t}^{i^*+1} \dots \mathbf{\Gamma}_{n,t}^{|\mathcal{T}_n|}]'$. Note that the number of MPCs will differ for each RX location and for each TX.

The above operation results in extracting 3 595 RX locations, as shown in Fig. 3c with one dot per location. The color codes refer to the number of transmitters from which the RX records channel measurements (annotated in the plot). Note that the RX records measurements from all TXs only when moving in area 4, whereas illumination from the four TXs is not uniform across the six areas.

V. EVALUATION

We proceed to evaluate the performance of our proposed scheme. First, we use the data collected at the NIST Boulder's campus, as presented in the previous section. Then, we extend the analysis to other scenarios by means of simulation, in order to explore the distribution of localization errors across an indoor space the impact of the number of TXs, the standard deviation of the AoA errors, and the size of the training dataset. We start the bootstrapping process by running the JADE algorithm on the full dataset. Due to uneven TX illumination, we cannot collect a sufficient number of AoAs (and therefore ADoAs) at some RX locations, especially in area 1 and area 3. In these cases, JADE cannot localize the RXs due to insufficient data. The remaining points where JADE can find a fix are ~ 2600 .

A. Illustration of the MPCs clustering operation

We start by discussing the performance and results of the clustering process outlined in Section III-C and Algorithm 1. As an example, consider one RX location within area 4. Fig. 4a shows a ray trace from TX-1, where we show the LoS MPC and first-order reflections reaching the RX. As expected, these MPCs spread over the full azimuthal angle domain due to the reflections from the perimeter of the room.

We compare this ray trace with the data from the measurements in Fig. 4b. Here, we illustrate the MPCs clustered from TX-1 in the delay-angle domain for the same RX location. Throughout our evaluation, we set the cluster radius $\epsilon = 3$, the number of neighbors $\gamma = 6$ and the scaling factor $\eta = 0.75$, chosen after an exhaustive search. For clarity, we portray the MPCs only in the delay and azimuth AoA domains, although we recall that elevation AoA values are also used as clustering features.

In Fig. 4b, we mark cluster centroids as black triangles (after the initial DBSCAN pass) and squares (after the recursive clustering procedure). As a first result, we observe that hierarchical reclustering is needed otherwise, e.g., the earliest arrivals having an AoA of 300° and above (in dark and light blue towards the top of the picture) would be mistaken as a single arrival. Each centroid can be interpreted as a dominant MPC. We numbered the most significant ones to illustrate that identified clustering include all key MPCs expected from the ray trace in panel (a). The centroid corresponding to the smallest MPC delay represents the LoS path (ray 1 in Fig. 4a), as confirmed by its AoA of about 250° . Similarly, MPC 2 has slightly larger AoA and delay features with respect to MPC 1; conversely, MPC 4 has a comparatively longer path length and an AoA of about 100° . The rest of the MPCs from TX-1 are annotated based on the scheme proposed in Section III-C.

From the azimuthal AoA features of the cluster centroids, we form the set of ADoAs values for the localization algorithm.

B. Performance evaluation for entire dataset

We now evaluate the performance of our tiny NN. We evaluate our model against JADE and other geometry-based

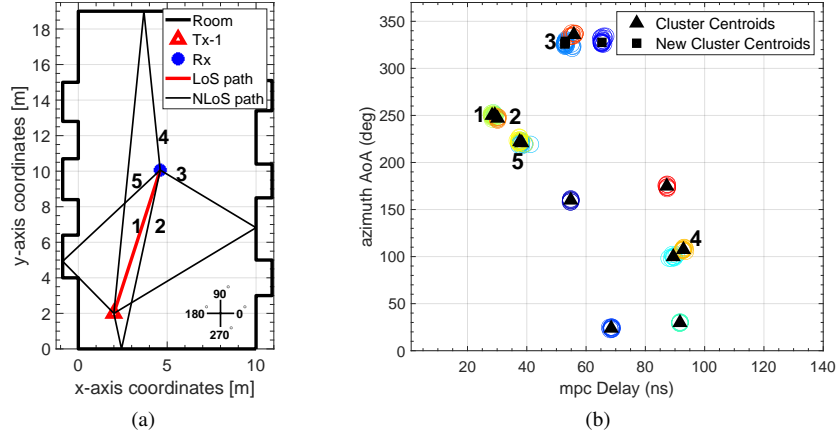


Fig. 4. MPCs clustering using our proposed recursive approach for a sample RX location in area 4. Note that the triangles represent the cluster centroids from the initial DBSCAN procedure and the squares represent the centroids obtained after recursive clustering. (a) Reference ray traces of the LoS and first-order MPCs from TX-1 to the RX. (b) Clustering of the MPCs from TX-1.

localization schemes. For this, we exploit the entire set of receiver locations across the room. Specifically, we initially run JADE on the entire dataset of ~ 2600 measurements to obtain the corresponding RX location estimates. Even when working on datasets with many measurements, some of JADE’s location estimates can be largely off. To avoid that such errors negatively affect the NN training process, we compute the centroid of all location estimates, fit a Gaussian distribution to the location estimates, and remove the 5% of all estimates that are farthest from the centroid. We then form a test set with 434 location labels and their corresponding ADoA features, and train the NN over the remaining points.

We illustrate the performance of our tiny NN through the cumulative distribution function (CDF) of the RX location error in Fig. 5, where we also compare our algorithm-supervised approach (referred to in the figures as AS-TNN) with the case when the NN model is trained with ground-truth location labels (referred to as TNN). Moreover, we also compare against JADE, the 2-hidden layer NN model proposed in [13], and the geometric scheme ADOA [18]. Our proposed NN model has (40, 36, 36, 18, 2) neurons respectively in each layer with the optimal hyperparameters $\kappa = 0.9$, $p = 0.2$, $r = 0.004$, and $b = 75\%$. We observe that our tiny algorithm-supervised NN performs similar to JADE. Both schemes achieve sub-meter localization accuracy in about 74% of the cases, with mean and median localization errors of about 86 cm and ~ 61 cm, respectively. On the other hand, the previous 2-hidden layer version of the tiny NN achieves sub-meter errors in 65% of the estimates, with the corresponding mean and the median errors being 98 cm and ~ 74 cm.

Our test environment entails a non-uniform distribution of RX locations across the room and a different number of ADoA measurements in each room area. In this case, adding a hidden layer improves the localization accuracy by learning a more complex relationship between ADoA values and the location of the RX. This contrasts the 2-layer NN in [13], which worked well only with uniform datasets and regular room shapes. We observe that our proposed models as well as the zero-knowledge algorithm JADE outperform the geometric

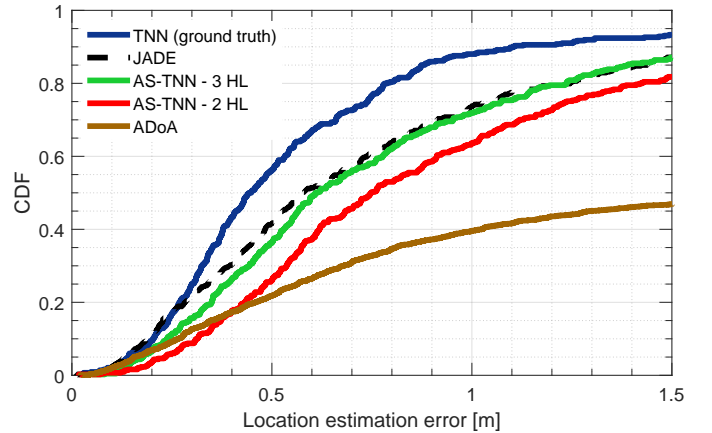


Fig. 5. CDF of the location estimation errors for our proposed 3-hidden layer (HL) NN (referred to as AS-TNN) against the previous 2-hidden layer model and other state-of-the-art algorithms. Note that our tiny NN trained with ground truth is referred to as TNN.

algorithm ADoA, that achieves sub-meter errors only in 40% of the cases.

When trained with true RX labels, the NN outperforms JADE, with sub-meter accuracy in about 88% of the cases, and a lower mean and median errors of 60 cm and ~ 45 cm. We emphasize that training the NN with ground-truth location labels is used here only to verify that the NN learns to accurately map ADoA measurements to the corresponding RX location. In practice, ground-truth locations would require a burdensome training dataset collection process, making our algorithm-supervised approach much more convenient. While JADE and our NN perform comparably in Fig. 5, JADE’s complexity increases as new measurements flow in [11], whereas the NN only requires a limited set of matrix multiplications and vector additions computed on a small-sized input set, once the training is complete.

To better understand the performance of our NN, we examine how localization errors distribute over different locations across the room. Fig. 6a codes localization error at each test location via a colored dot, where blue hues represent low or

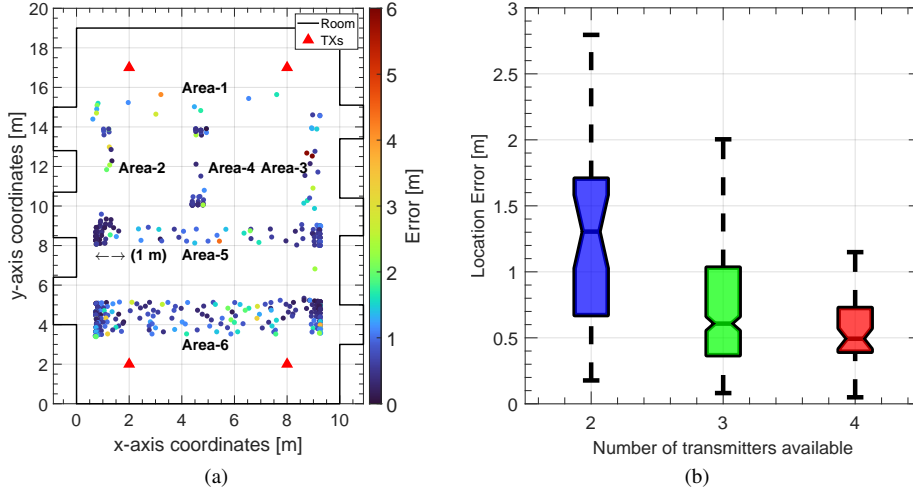


Fig. 6. Localization error for all regions with different number of transmitters available. (a) Location-wise performance of algorithm-supervised tiny NNs at the test locations (b) Statistical dispersion of the location error for regions having different numbers of available transmitters.

acceptable errors. We observe localization errors of < 1 m at the majority of the test locations, mostly in areas 2, 4, 5, and 6. There are two reasons behind this result. First, the RX moving in these areas receives signals from 3 or 4 TXs. This yields a larger number of clustered MPCs, thus a larger number of input ADoA values. The greater the number of ADoAs per location, the more accurately JADE and the NN can localize the RX. Secondly, these areas include a larger number of RX measurements available compared to areas 1 and 3, and constitute a larger proportion of the training data. Thus, the model can estimate the location of the RX with better accuracy. On the contrary, large estimation errors in areas 1 and 3 tend to be larger. This is because the RX records measurements only from two transmitters, and the set of measurement locations is sparser compared to other areas. However, many locations in these areas still yield sub-meter errors, implying that both JADE and our algorithm-supervised NN infer the relationship between ADoAs and RX locations even by observing a limited number of examples.

Fig. 6b summarizes the above observations by showing the statistical dispersion of the location estimation error for different regions, as a function of the number of available TXs. The median localization error decreases with increasing number of transmitters, and the greatest improvement is attained when transitioning from two to three available TXs. The dispersion of the error also decreases: the whiskers of the boxplots span progressively smaller intervals for increasing number of transmitters, and the highest errors occur only in areas with two transmitters. Although the number of RX locations in the training and test sets is heavily biased towards regions with three available TXs, we still observe a general trend of decreasing localization errors with increasing number of transmitters. This is because the bootstrapping algorithm JADE can localize the RX more reliably when observing more ADoA measurements. In these cases, the NN will also be able to map the ADoAs to the RX location more accurately.

C. Performance evaluation over different areas

We now discuss the performance of our NN when trained with a smaller training dataset. To do this, we leverage the diversity of measurements recorded during the campaign, where both the number of available TXs and the number of measurements collected vary across different areas. We choose three diverse sections: areas 2, 3 and 4, which occupy the top half of the room; area 5, that spans the room horizontally towards the middle; and area 6, which spans the bottom side. In areas 2, 3, and 4, the dataset includes measurements from 455 RX locations. Note that we consider these areas together, as otherwise JADE would not observe sufficiently many measurements to yield accurate estimates. The number of measurements in area 5 is slightly higher, with 593 valid locations. Finally, 1396 RX measurements are available in area 6. In all the three scenarios, we enact a 20%–80% split between the test set and the training set.

Fig. 7 shows the CDF of the localization error attained by our NN and by JADE. As previously observed, the NN model learns the mapping between ADoAs and the bootstrap location labels even with limited measurements, and matches the performance of JADE well in all scenarios. This opens the opportunity to train different tiny NNs for different areas, depending on the number of available TXs. This would improve the localization coverage, especially in large and distributed indoor environments. We leave this extension as a future development of our research.

Notice that the performance of both JADE and the NN are better in areas 2, 3 and 4 as well as area 5, and more erroneous in area 6. This is a consequence of resorting to an algorithm-supervised approach, which inherently achieves the best performance only when the bootstrapping algorithm is also accurate throughout a given area. In our case, JADE performed remarkably good in areas 2, 3 and 4 as well as area 5. Here, the NN is trained with low-error location labels, and therefore performs well. Conversely, JADE's location labels are affected by larger errors in area 6. This affects the

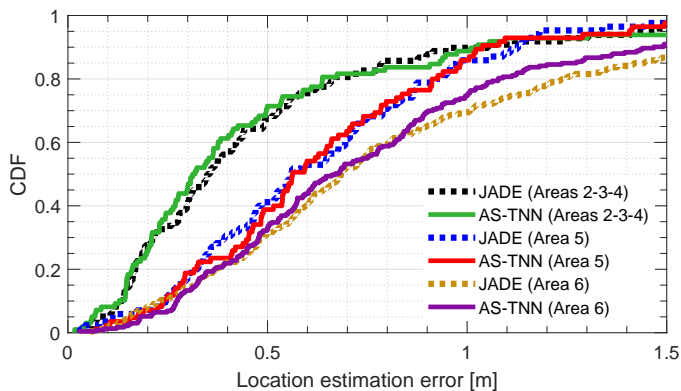


Fig. 7. CDF of the location estimation errors for our proposed 4-layer NN when trained and tested in three scenarios: (i) in Areas 2, 3, and 4; (ii) in Area 5; and (iii) in Area 6.

training of the NN, which achieves sub-meter errors in 75% of the cases, instead of, e.g., 85% for area 5.

Compare now against the performance of the NN trained with ground-truth location labels: we observe that the overall accuracy loss when the bootstrapping algorithm is accurate (such as in areas 2, 3 and 4, or in area 5) brings the proportion of locations with sub-meter errors from about $\approx 90\%$ to $\approx 85\%$. If the bootstrapping algorithm is less accurate (e.g., like JADE working on data from area 6), the proportion decreases to about 75%. Even though area 6 provides the largest number of dataset points, compounding training data from all areas increases the localization performance of the NN with respect to training on data from area 6 alone.

D. Impact of number of hidden layers and clustering of MPCs

We now turn to assessing the impact of the number of hidden layers in the NN, as this parameter affects the computational complexity. Fig. 8 presents the statistical dispersion of localization errors for varying number of hidden layers in the tiny NN model. Specifically, we vary from 2 hidden layers (as proposed in [13]) to 6. We observe a decrease in the median error from ~ 76 cm to ~ 60 cm as we move from a 2-HL model to a 3-HL model. As more layers are added to the model, the whiskers of the boxplot span almost the same interval, implying a similar performance as a 3-HL model. We also note that, as the number of layers increases, the NN will be able to represent a more complex regression function, but at a cost of learning and tuning more parameters. Moreover, adding hidden layers may lead to more accurate localization, it would also increase the computational complexity of NN training and inference. As our primary goal is to learn the smallest NN model that can match the performance of JADE, we limit our search to a 3-layer model.

To understand the impact of clustering the MPCs on the localization performance, we propose to feed JADE and our NN model with ADoAs obtained after both regular and our proposed recursive DBSCAN procedure. Fig. 9 presents the CDF of the localization errors incurred by JADE as well as our algorithm-supervised tiny NN model when using ADoAs obtained from the two procedures. While the NN model is able

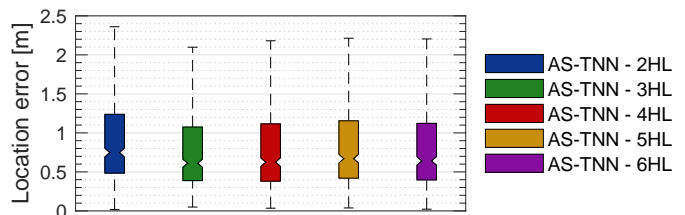


Fig. 8. Statistical dispersion of localization errors for varying number of hidden layers in the tiny NN. Here, AS-TNN - k HL denotes our algorithm-supervised tiny NN with k hidden layers.

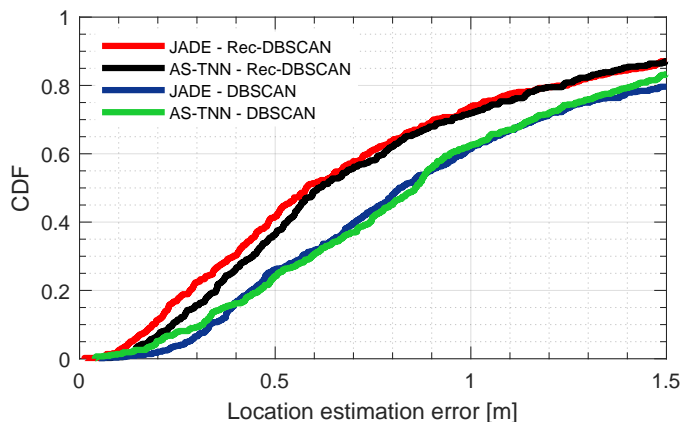


Fig. 9. CDF of the location errors when using the dominant MPCs obtained from the regular DBSCAN and the proposed recursive DBSCAN (here, Rec-DBSCAN).

to match the performance of the bootstrapping localization algorithm in both the cases, we can clearly observe an increase in the sub-meter localization errors from 61% to 74% when recursively clustering the MPCs. This is because recursive DBSCAN finely breaks down large clusters, resulting in rich set of ADoA measurements corresponding to the dominant MPCs reflected off the walls. This significantly improves JADE's performance, and subsequently that of the TNN.

E. Complexity analysis of the tiny NN

We now evaluate the complexity of our NN model using the following two metrics:

Number of Parameters. The computational complexity of a fully connected NN is determined by the total number of parameters (i.e., the weights and biases) that the model learns during the training phase. For a fully connected NN, the overall computational complexity is usually given as $\mathcal{O}(\sum_{k=1}^L n_k \cdot m_k)$, where n_k and m_k are the number of input and output neurons in layer k of the NN. Our tiny NN architecture comprises (40, 36, 36, 18, 2) neurons respectively in each layer, resulting in an overall complexity of $\mathcal{O}(3420)$, and the number of trainable parameters equalling 3512. In case of our bootstrapping algorithm JADE, the complexity of the initial grid search problem is $\mathcal{O}(|\mathcal{A}|^2 2^{16})$, where \mathcal{A} represents the total number of anchors. Each of the subsequent iterative MMSE problems have the quadratic complexity that depends on the number of anchors, number of iterations needed to converge, and the number of measurements.

Mean training and testing times. We perform preliminary experiments to evaluate the mean training and inference times of our NN model. For this, we used a Thinkpad E14 laptop, with an AMD Ryzen 7 4000 CPU and 24 GBytes of RAM, running in battery-saver mode. Our NN model takes an average of ~ 165 s to train, and the mean inference time is about 1.22 ms. Running JADE on the same machine takes about 1400 s (about 23 mins) to obtain the training labels. This is because JADE solves a large grid search problem having 2^{16} points, followed by computationally intensive iterative solution of two inter-dependent MMSE problems. Thus, from a systems perspective, we propose to offload JADE and the NN training process to an edge server.

We remark that as the indoor scenario becomes more complex (i.e., with more obstacles, complex-shaped rooms, additional APs, etc.), the number of MPCs between the TX and the RX will increase. To accurately localize the client, our bootstrapping localization algorithm will have to incorporate more measurements for each location, and process them altogether with a higher degree of computational complexity. As the input to both schemes is the same, the NN model would require more parameters as well, in order to learn the mapping between the measurements and the location labels. This can be achieved by increasing the model’s complexity, such as by adding more hidden layers or using convolutional layers. Note that, this will directly impact the computational complexity of the NNs.

F. Simulation study of localization error distribution

We now complement the above results by analyzing the performance of our model in an indoor environment via simulation. Fig. 10a illustrates an 11 m \times 12 m H-shaped room consisting of two 4 m \times 12 m rectangular sections and a 3 m \times 6 m section in the middle. We deploy five mmWave TXs at coordinates (2, 2), (2, 10), (5.5, 6), (9, 2), and (9, 10). Blue squares convey a few first-order VAs with respect to each wall of the room.

We simulate a set of mobile RX trajectories in the indoor environment to generate training data for the NN. Each of the trajectories comprises 30 RX locations. We collect the set of AoAs at each location from all transmitters and the VAs using a ray tracer. In order to produce results that mimic realistic scenarios with imperfect AoA estimation, we perturb the AoAs with zero-mean Gaussian noise of standard deviation $\sigma = 5^\circ$. In total, we generate 1500 RX locations. A subset of these locations will be used to train and test our model as detailed below.

As in Section V-B, we run JADE on the whole dataset and remove the 5% of the location estimates that are farthest from the centroid of all estimates. This results in keeping 1425 client locations, of which 475 locations constitute the test set. After hyperparameter optimization, the NN model has (40, 36, 36, 18, 2) neurons in each layer with $\kappa = 0.9$, $p = 0.1$, $r = 0.003$, and $b = 50\%$.

Fig. 10b shows the CDF of the location error as estimated using JADE and the algorithm-supervised NN. We observe that the NN performs as good as JADE with sub-meter location accuracy in about 92% of the cases, with

slightly better performance for errors less than 50 cm. For comparison, 98% of the estimates yield an error of < 1 m when the NN is trained with true locations. These results are significantly good for two main reasons: because JADE can work with a comparatively large measurement set, and because each measurement location is illuminated by multiple MPCs. Bootstrapping with accurate location labels from JADE thus improves the performance of the NN.

Fig. 10c illustrates the localization error heat map in the H-shaped room, for all test locations, as estimated using the algorithm-supervised NN. Blue hues represent low estimation errors (< 1 m), light blue to green hues represent errors between 1 m and 2 m, whereas yellow to red hues convey errors between 3 m and 6 m. The results confirm that the localization error is < 1 m throughout the room, except for slightly higher errors in the bottom-right section. A similar situation occurs near the top-right corner of the middle section. The main reason is that the training dataset is not collected at uniformly distributed locations, and may thus be sparser in some areas, which also explains why the heat map is not symmetrical.

Fig. 11 explores how reducing the number of transmitters affects the localization. In Fig. 11a, we observe that removing the middle TX reduces the illumination at the corner areas and thus increases localization errors. This includes both the LoS MPCs and NLoS MPCs originating from reflections on the left and right side walls, as well as the top and bottom walls of the middle section. Removing one additional TX, e.g., the top right one, leads to higher localization errors in its surroundings (Fig. 11b). However, the removal affects the whole room, as the TX helps illuminate other room sections through the NLoS MPCs reflecting off the right wall of the room and the bottom wall of the central section.

Finally, Fig. 12 discusses the effect of a lower AoA estimation accuracy, i.e., an error of $\sigma = 7^\circ$ affecting AoA values. For this, we consider the initial room setup with 5 TXs, and evaluate the impact of training set size on localization. Fig. 12a presents the same scenario as in Fig. 10c, with $\sigma = 7^\circ$. We observe a general error increase, where the central sections of the room are still remarkably well represented by the learned NN model, whereas worse errors tend to concentrate at the corner sections. We stress that such a large σ means that about 95% of the AoAs span an interval of $\pm 14^\circ$ from the true value. Consider the case of a RX located at any far corner of the room: a 14° error on the AoA of the LoS path from the farthest TX would result in an offset in the RX’s own location estimate of ~ 3 m (measured along the circumference centered on that TX with radius equal to the TX–RX distance).

We expect that the more examples the NN sees from the bootstrapping algorithm, the higher the chances that some location estimates bear a small error. Fig. 12b shows that, in order to reduce the localization error to levels comparable with Fig. 10c, we need to increase the training set (about 3 times the size used for Fig. 12a in our scenario). With this, we achieve sub-meter errors almost everywhere, except for a few locations close to the room corners.

In general our performance evaluation shows that a tiny algorithm-supervised NN can accurately localize a user in

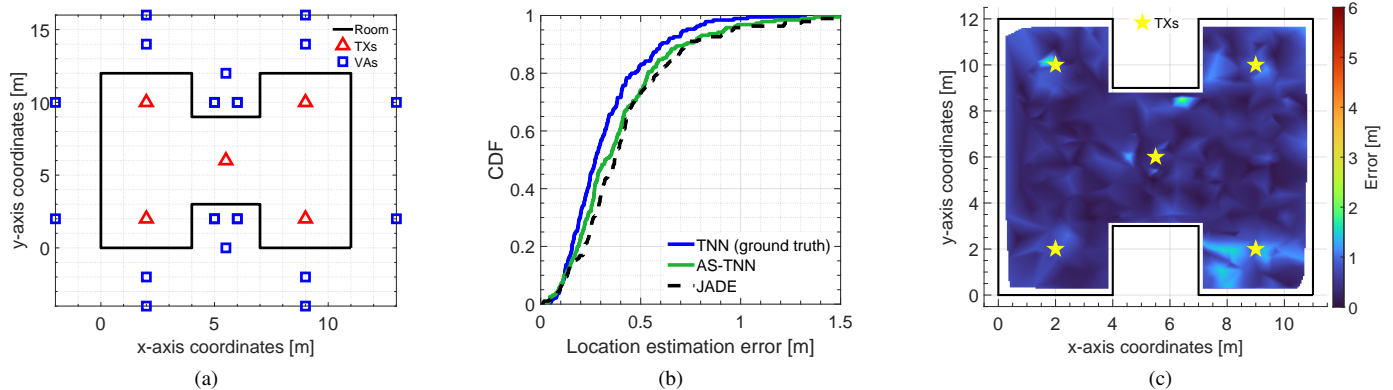


Fig. 10. (a) H-shaped room environment. Note the different axis scale. (b) CDF of location estimation error in the H-shaped room. (c) Heat map of the localization errors for the H-shaped room with 5 TXs.

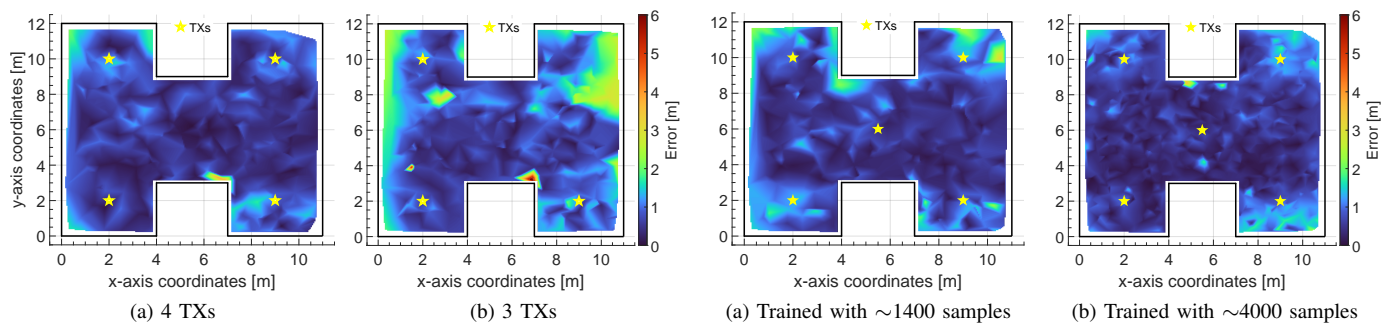


Fig. 11. Heat map of the localization errors for the H-shaped room for different numbers of transmitters, $\sigma = 5^\circ$.

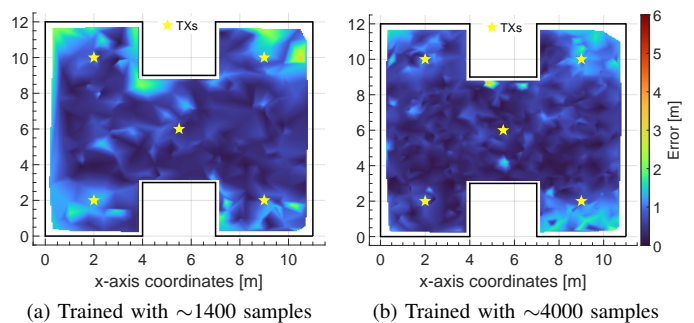


Fig. 12. Heat map of the localization errors for the H-shaped room, for AoA error standard deviation $\sigma = 7^\circ$ and different NN training set sizes.

a complex indoor environment in the presence of two key factors: *i*) richness of input features, coming either from LoS paths, NLoS paths, or both; and *ii*) richness of training data, so that the NN observes sufficiently many error-prone samples.

VI. DISCUSSION AND CONCLUSIONS

We presented an algorithm-supervised approach to train a tiny NN to localize a mmWave device using ADoA measurements in an indoor environment. This relieves the burdensome task of collecting training data by harvesting location labels from a bootstrapping localization algorithm. We evaluated the performance of our scheme via channel measurements from a NIST mmWave channel sounder. The channel measurements were processed using the SAGE algorithm to obtain all the MPCs at the receiver. We emphasize that, to the best of our knowledge, this is the first algorithm that processes a full, rich, and complex indoor channel information rather than using information pre-filtered by other algorithms or device firmwares. To identify dominant MPCs reflected off different surfaces, we proposed a recursive clustering algorithm based on DBSCAN. The azimuthal AoAs associated with the cluster centroids were used to compute ADoAs. Our performance evaluation shows that tiny NNs can accurately estimate the location of the receiver when trained with true locations. While the error inevitably increases in the algorithm-supervised case, our scheme still achieves sub-meter error in about 75% of the cases, with a much lower computational complexity than the

bootstrapping algorithm. Additional simulation results confirm that the key elements that enable high accuracy are richness of illumination from multiple MPCs and training data.

Our future work will address several challenges. One key challenge is to develop schemes that can automatically decide when to switch between the bootstrapping algorithm JADE and the tiny NN model. It is crucial to run JADE only up to the point where its computational complexity remains within acceptable limits for real-time environments. Automatically determining this optimal point will facilitate seamless transitions between the two schemes during runtime. Additionally, we will focus on developing techniques to dynamically associate AoAs of dominant MPCs with ambient scatterers and anchors in more complex and dynamic indoor environments. Unlike our current indoor setup, dynamic scatterers in complex-shaped rooms can result in a large number of anchors. Correctly associating the ADoAs in such environments will be crucial for both the bootstrapping algorithm and the NN. Addressing these challenges will further improve robustness and accuracy in general indoor scenarios.

REFERENCES

- [1] F. Lemic, J. Martin, C. Yarp, D. Chan, V. Handziski, R. Brodersen, G. Fettweis, A. Wolisz, and J. Wawrzyn, "Localization as a feature of mmWave communication," in *Proc. IWCMC*, 2016.
- [2] H. Wymeersch and G. Seco-Granados, "Radio localization and sensing—Part I: Fundamentals," *IEEE Commun. Lett.*, 2022.
- [3] U. T. Virk and K. Haneda, "Modeling human blockage at 5G millimeter-wave frequencies," *IEEE Trans. Antennas Propag.*, no. 3, 2020.

- [4] I. A. Hemadeh, K. Satyanarayana, M. El-Hajjar, and L. Hanzo, "Millimeter-wave communications: Physical channel models, design considerations, antenna constructions, and link-budget," *IEEE Commun. Surveys Tuts.*, no. 2, 2018.
- [5] A. Shastri, N. Valecha, E. Bashirov, H. Tataria, M. Lentmaier, F. Tufveson, M. Rossi, and P. Casari, "A review of millimeter wave device-based localization and device-free sensing technologies and applications," *IEEE Commun. Surveys Tuts.*, no. 3, 2022.
- [6] S. Sur, I. Pefkianakis, X. Zhang, and K.-H. Kim, "Towards scalable and ubiquitous millimeter-wave wireless networks," in *Proc. ACM MobiCom*, 2018.
- [7] J. Palacios, P. Casari, H. Assasa, and J. Widmer, "LEAP: Location estimation and predictive handover with consumer-grade mmWave devices," in *Proc. IEEE INFOCOM*, 2019.
- [8] C. Fiandrino, H. Assasa, P. Casari, and J. Widmer, "Scaling millimeter-wave networks to dense deployments and dynamic environments," *Proceedings of the IEEE*, no. 4, 2019.
- [9] J. Yang, J. Xu, X. Li, S. Jin, and B. Gao, "Integrated communication and localization in millimeter-wave systems," *Frontiers of Information Tech. & Electronic Eng.*, no. 4, 2021.
- [10] Z. Xiao and Y. Zeng, "An overview on integrated localization and communication towards 6G," Dec. 2021.
- [11] J. Palacios, P. Casari, and J. Widmer, "JADE: Zero-knowledge device localization and environment mapping for millimeter wave systems," in *Proc. IEEE INFOCOM*, 2017.
- [12] I. Pefkianakis and K.-H. Kim, "Accurate 3D localization for 60 GHz networks," in *Proc. ACM SenSys*, 2018.
- [13] A. Shastri, J. Palacios, and P. Casari, "Millimeter wave localization with imperfect training data using shallow neural networks," in *Proc. IEEE WCNC*, 2022.
- [14] S. Blandino, J. Senic, C. Gentile, D. Caudill, J. Chuang, and A. Kayani, "Markov multi-beamtracking on 60 GHz mobile channel measurements," *IEEE Open J. of Veh. Technol.*, 2022.
- [15] F. Zafari, A. Gkelias, and K. K. Leung, "A survey of indoor localization systems and technologies," *IEEE Commun. Surveys Tuts.*, no. 3, 2019.
- [16] M. Vari and D. Cassioli, "mmWaves RSSI indoor network localization," in *Proc. IEEE ICC*, 2014.
- [17] A. Olivier, G. Bielsa, I. Tejado, M. Zorzi, J. Widmer, and P. Casari, "Lightweight indoor localization for 60-GHz millimeter wave systems," in *Proc. IEEE SECON*, 2016.
- [18] J. Palacios, G. Bielsa, P. Casari, and J. Widmer, "Single-and multiple-access point indoor localization for millimeter-wave networks," *IEEE Trans. Wireless Commun.*, no. 3, 2019.
- [19] A. Blanco, P. J. Mateo, F. Gringoli, and J. Widmer, "Augmenting mmWave localization accuracy through sub-6 GHz on off-the-shelf devices," in *Proc. ACM Mobisys*, 2022.
- [20] O. Kanhere, S. Ju, Y. Xing, and T. S. Rappaport, "Map-assisted millimeter wave localization for accurate position location," in *Proc. IEEE GLOBECOM*, 2019.
- [21] A. Yassin, Y. Nasser, M. Awad, and A. Al-Dubai, "Simultaneous context inference and mapping using mm-Wave for indoor scenarios," in *Proc. IEEE ICC*, 2017.
- [22] A. Yassin, Y. Nasser, and M. Awad, "Geometric approach in simultaneous context inference, localization and mapping using mm-Wave," in *Proc. ICT*, 2018.
- [23] A. Yassin, Y. Nasser, A. Y. Al-Dubai, and M. Awad, "MOSAIC: Simultaneous localization and environment mapping using mmWave without a-priori knowledge," *IEEE Access*, 2018.
- [24] J. Palacios, G. Bielsa, P. Casari, and J. Widmer, "Communication-driven localization and mapping for millimeter wave networks," in *Proc. IEEE INFOCOM*, 2018.
- [25] G. Bielsa, J. Palacios, A. Loch, D. Steinmetzer, P. Casari, and J. Widmer, "Indoor localization using commercial off-the-shelf 60 GHz access points," in *Proc. IEEE INFOCOM*, 2018.
- [26] T. T. Tsai, L. H. Shen, C. J. Chiu, and K. T. Feng, "Beam AoD-based Indoor Positioning for 60 GHz mmWave System," in *Proc. IEEE VTC-Fall*, 2020.
- [27] A. Washist, D. R. Bhanushali, R. Relyea, C. Hochgraf, A. Ganguly, P. D. Sai Manoj, R. Ptucha, A. Kwasinski, and M. E. Kuhl, "Indoor wireless localization using consumer-grade 60 GHz equipment with machine learning for intelligent material handling," in *Proc. IEEE ICCE*, 2020.
- [28] M. Pajovic, P. Wang, T. Koike-Akino, H. Sun, and P. V. Orlik, "Fingerprinting-based indoor localization with commercial mmWave WiFi - Part I: RSS and beam indices," in *Proc. IEEE GLOBECOM*, 2019.
- [29] P. Wang, M. Pajovic, T. Koike-Akino, H. Sun, and P. V. Orlik, "Fingerprinting-based indoor localization with commercial mmWave WiFi - Part II: Spatial beam SNRs," in *Proc. IEEE GLOBECOM*, 2019.
- [30] T. Koike-Akino, P. Wang, M. Pajovic, H. Sun, and P. V. Orlik, "Fingerprinting-based indoor localization with commercial mmWave WiFi: A deep learning approach," *IEEE Access*, 2020.
- [31] P. Wang, T. Koike-Akino, and P. V. Orlik, "Fingerprinting-based indoor localization with commercial mmWave WiFi: NLOS propagation," in *Proc. IEEE GLOBECOM*, 2020.
- [32] P. Hong, C. Li, H. Chang, Y. Hsueh, and K. Wang, "WBF-PS: WiGig beam fingerprinting for UAV positioning system in GPS-denied environments," in *Proc. IEEE INFOCOM*, 2020.
- [33] Z. Wei, Y. Zhao, X. Liu, and Z. Feng, "DoA-LF: A location fingerprint positioning algorithm with millimeter-wave," *IEEE Access*, 2017.
- [34] C. Lai, R. Sun, C. Gentile, P. B. Papazian, J. Wang, and J. Senic, "Methodology for multipath-component tracking in millimeter-wave channel modeling," *IEEE Trans. Antennas Propag.*, no. 3, 2019.
- [35] A. F. Molisch, *Wireless communications*. John Wiley & Sons, 2012, ch. 7.
- [36] C. Gentile, P. B. Papazian, R. Sun, J. Senic, and J. Wang, "Quasi-deterministic channel model parameters for a data center at 60 GHz," *IEEE Antennas Wireless Propag. Lett.*, no. 5, 2018.
- [37] M. Ester, H.-P. Kriegel, J. Sander, X. Xu *et al.*, "A density-based algorithm for discovering clusters in large spatial databases with noise," in *Proc. AAAI KDD*, no. 34, 1996.
- [38] C. Lai, R. Sun, C. Gentile, P. B. Papazian, J. Wang, and J. Senic, "Methodology for multipath-component tracking in millimeter-wave channel modeling," *IEEE Trans. Antennas Propag.*, no. 3, 2019.
- [39] J. Wang, C. Gentile, J. Senic, R. Sun, P. B. Papazian, and C. Lai, "Unsupervised clustering for millimeter-wave channel propagation modeling," in *Proc. IEEE VTC-Fall*, 2017.
- [40] H. Tsukada, K. Kumakura, S. Tang, and M. Kim, "Millimeter-wave channel model parameters for various office environments," *IEEE Access*, vol. 10, pp. 60 387–60 396, 2022.
- [41] R. Sun, P. B. Papazian, J. Senic, Y. Lo, J.-K. Choi, K. A. Remley, and C. Gentile, "Design and calibration of a double-directional 60 GHz channel sounder for multipath component tracking," in *Proc. EUCAP*, 2017.
- [42] K. Hausmair, K. Witrals, P. Meissner, C. Steiner, and G. Kail, "SAGE algorithm for UWB channel parameter estimation," in *COST 2100 Committee Meeting*, 2010.